

# Growth dynamics and amorphous-to-crystalline phase transformation in natural nacre

Laura Otter (✉ [Laura.Otter@anu.edu.au](mailto:Laura.Otter@anu.edu.au))

The Australian National University <https://orcid.org/0000-0003-0737-4497>

Katja Eder

The University of Sydney

Matt Kilburn

The University of Western Australia

Limei Yang

University of Sydney

Padraic O'Reilly

Molecular Vista (United States)

Derek Nowak

Molecular Vista, San Jose

Julie Cairney

The University of Sydney <https://orcid.org/0000-0003-4564-2675>

Dorrit Jacob

The Australian National University <https://orcid.org/0000-0003-4744-6627>

---

## Article

### Keywords:

**Posted Date:** July 5th, 2022

**DOI:** <https://doi.org/10.21203/rs.3.rs-1810421/v1>

**License:**  This work is licensed under a Creative Commons Attribution 4.0 International License.

[Read Full License](#)

---

**Version of Record:** A version of this preprint was published at Nature Communications on April 20th, 2023. See the published version at <https://doi.org/10.1038/s41467-023-37814-0>.

# Abstract

Biominerals, such as nacreous bivalve shells, are important archives of environmental information. The processes explaining how the organisms code this information into the structure and composition of their shells are yet unknown. Most marine calcifiers form their shells from amorphous calcium carbonate by particle attachment and stepwise crystallisation of metastable precursor phases. However, the mechanism of this transformation including its incorporation of trace metal ions used for environmental reconstructions are poorly constrained. Using the nacreous shell of the Mediterranean mussel, we explore the formation of nacre from the meso- to the atomic scale. We use a novel combination of strontium pulse-chase labelling in aquaculture experiments and correlative micro- to sub-nanoscale analysis to show that nacre grows in a two-step process and crystallizes via localised dissolution and reprecipitation within nanogranules. Our findings elucidate how stepwise crystallization pathways affect trace element incorporation in natural biominerals, while preserving their intricate hierarchical structure.

## Introduction

A growing body of evidence indicates that calcifying organisms form their hard parts (e.g., shells) from amorphous calcium carbonate (ACC), which later transforms via a step-wise crystallization of intermediate metastable phases rather than by direct precipitation of aragonite and calcite from seawater<sup>1,2</sup>. Observations of ACC in natural bio-carbonate systems such as echinoid spicules<sup>3</sup>, foraminifera shells<sup>4</sup> and mollusc nacre<sup>4,5</sup> were among the main drivers of the paradigm change in crystallization theory from classical monomer-by-monomer processes towards non-classical crystallization pathways<sup>6</sup>. In fact, crystallization via particle attachment and stepwise transformation of metastable precursor phases are now recognized as crystallization mechanisms for many different systems<sup>2,6,7</sup>.

Bio-carbonates are important archives for both environmental reconstructions and forward-modelling of future environmental and climatic conditions, including sea-surface temperatures, ocean pH and salinity<sup>8-10</sup>. Presently, these reconstructions are based on the incorrect assumption that bio-calcite and -aragonite form directly via precipitation from seawater and more realistic modelling of uptake and distribution of elements and isotopes via a stepwise crystallization pathway via ACC is still lacking.

A critical knowledge gap in working towards a new model for element and isotope partitioning in natural bio-carbonates is the lack of insight into the mechanisms by which the different intermediate calcium carbonate phases control the chemical composition of the final stable phase. Generally, the composition of crystalline phases is governed by their distinct crystal chemistry and can be quantified using equilibrium partition coefficients, defined as the concentration ratio of a specific element between two phases<sup>11</sup>. Amorphous calcium carbonate (ACC), the first solid phase formed in bio-carbonates, incorporates elements indiscriminately<sup>12,13</sup>. Upon stepwise crystallization, ACC transforms into new phases via dissolution and reprecipitation, solid-solid transformation, or a combination thereof<sup>14</sup>. While

dissolution and reprecipitation mechanisms are governed by equilibrium partition coefficients<sup>11,15,16</sup>, chemical re-distribution during solid-solid transformation can deviate significantly from equilibrium partitioning and instead preserves the original chemical composition of ACC in the crystalline end-product. Thus, either transformation pathway has a significantly different effect on element partitioning into the final crystalline phase.

In the laboratory, ACC typically transforms via a dissolution and reprecipitation mechanism<sup>14,15,17,18</sup>. This pathway is usually associated with significant morphological changes to the texture of the solid phase<sup>14-16</sup>. However, preservation of intricate hierarchical structural details in natural systems (e.g., Jacob et al.<sup>19</sup>) during stepwise crystallization seems to contradict the findings in the laboratory, but supports either solid-state transformation, or very localized dissolution-reprecipitation processes.

We aim here to elucidate the transformation mechanisms from ACC to aragonite during bivalve nacre growth using living Mediterranean mussel (*Mytilus galloprovincialis*) shells and a novel combination of Sr pulse chase labelling experiments with correlated micro- to sub-nanometre analysis of nacre. *M. galloprovincialis* shells form via a step-wise crystallization pathway from ACC to aragonite<sup>4,12,20</sup>. Pulse-chase labelling of living bivalves in aquaculture (see methods) produces shells with well-defined bands of Sr-enriched CaCO<sub>3</sub> that serve as visual 'timestamps' of shell growth<sup>21</sup>. Aquaculture-based pulse-chase labelling experiments employing trace elements like strontium and magnesium have significantly furthered our understanding of the growth dynamics in various corals and sea urchins<sup>22-24</sup>, yet, similar applications to bivalves are rare<sup>21</sup>. Correlative analysis using Nanoscale Secondary Ion Mass Spectrometry (NanoSIMS), Atom Probe Tomography (APT) and nano-scale Photo-induced Force Microscopy (PiFM) enabled stepwise spatially downscaled visualization of the 'time stamped' nacre portions for the first time down to the atomic scale. We show that nacre forms via a two-stepped process of extensional followed by space-filling growth, a process that has long been suggested but is observed here directly for the first time. Most importantly, we demonstrate that the transformation of ACC to aragonite in natural nacre occurs via dissolution and reprecipitation within individual nanogranules, thus elucidating the mechanism behind preservation of the hierarchical nanostructures in natural biominerals upon stepwise crystallization.

## Results

### Nacre growth visualized by strontium pulse-chase labelling

The aragonitic nacreous shell layer in *M. galloprovincialis* is the innermost of two calcified layers (Fig. 1) and contains up to 3 wt.% of a wide variety of organic molecules<sup>25</sup>, which provide an architectural framework<sup>26</sup> and control mineralization<sup>27</sup>. Both, CaCO<sub>3</sub> and organics are secreted by the epithelial cells of the organism's mantle tissue which covers the entire inner surface of the shell. Mature nacre consists of ca. 10–20 µm wide and 0.5 µm thick polygonal aragonite tablets which are individually enveloped in organic sheaths of ca. 30 nm thickness<sup>25,28</sup>. In addition, significant amounts of organic inclusions sized

2–25 nm are included in each nacre tablet<sup>25,29</sup>. Nacre grows via ACC particles of ca. 20–150 nm in size secreted by the epithelial tissue into a framework of organic sheets, creating a characteristic nanogranular structure<sup>30–33</sup>. New layers of nacre are added via mineral bridges through pores in the organic sheets<sup>28,34–37</sup> and progressively transform into aragonite upon ageing<sup>1,4,5,20</sup>.

Bivalve shells grown during our pulse-chase labelling aquaculture experiment have differences in Sr concentrations of 10,434 µg/g between labelled and unlabelled nacre portions (see methods, Supplementary Tables 1 and 2) which translate into Sr-labelled shell portions appearing as lighter grey nacre layers in-between the darker grey portions of unlabelled shell in Backscattered Electron (BSE) images (Fig. 1; Supplementary Fig. 1). Natural variations in growth rates between individual bivalves result in different widths of labelled shell portions within and between individual bivalve shells<sup>21</sup>. Here, we selected specimens for further high-resolution analysis that had the highest growth to achieve best spatial resolution (Supplementary Table 1).

At the micron- to nanoscale, NanoSIMS isotope ratio distribution maps of the nacre in Sr labelled shells (Fig. 2a) show a stepped growth pattern along the nacre growth with regions of distinctly high Sr/Ca ratios (warm colours in Fig. 2) intercalated with areas of low Sr/Ca ratios (blue colours). Abrupt high angle changes in colour from magenta to blue and *vice versa* in the maps mark the transitions from labelled to unlabelled tablet portions (Fig. 2b, white arrowheads). Transitions between high and low Sr/Ca areas cut through individual tablets (Fig. 2b). Green to yellow pixels along these transitions reflect intermediate Sr/Ca ratios, likely representing concentration mixtures beyond the spatial resolution of individual pixels (see methods).

Using the timestamps created by Sr labelling, we can differentiate two nacre growth directions at sub-micrometre length scales: *extensional growth* forms new nacre layers along the inner shell surface and progresses quasi-simultaneously at multiple locations of different tablets, normal to the organic interlamellar sheets (in Fig. 2c, white arrows). This is followed by *space-filling nacre growth* parallel to the organic interlamellar sheets (Fig. 2c, grey arrows; Supplementary video) which proceeds via incremental additions of CaCO<sub>3</sub> nanogranules to the growing nacre tablets. This two-stepped mode of growth, consisting of an extensional followed and a space-filling growth component, was previously observed for corals<sup>38</sup> and was inferred for molluscs<sup>26,39</sup>, but this study is the first direct observation of this process in bivalve shells.

## Strontium zonation in nano-granules

We used Atom Probe Tomography (APT) to explore atomic-scale element distribution patterns in Sr-labelled nacre. We prepared regions of interest in the Sr-enriched shell portion with the interlamellar organic sheet as a point of reference for APT-tip preparation using our newly developed methodology of BSE imaging during Focussed Ion Beam (FIB) cutting (see methods and Supplementary Fig. 3).

We analysed three different areas in one APT tip (Supplementary Fig. 4). The colour-coded 3D APT reconstructions (Fig. 3, Supplementary Fig. 5 to 8) show the Ca-rich mineral phase of the nacre tablets in grey to the left, while high concentrations of C (magenta) and H (yellow) identify the organic interlamellar sheet to the right (Fig. 3a, b). A cortex of ca. 3.8 nm in thickness, significantly enriched in Sr, is situated on the outer area of the nacre tablet adjacent to the interlamellar sheet (Fig. 3c, d). The location of this Sr-enriched cortex neighbouring, but not co-located with the organic sheet is best visible in the atom probe concentration profile (Fig. 4). The other reconstructed regions of the tip (Supplementary Fig. 5 to 8) show comparable results with significantly enriched Sr cortices of similar thicknesses (4.5 nm and 5.0 nm) adjacent to the organic sheet.

Sodium concentrations increase towards the organic interlamellar sheet with some detectable Na enrichment in the organic material (Fig. 3e, 4, Supplementary Fig. 6 to 8). Similar Na-enrichment in the organic layers in natural bio-carbonate were reported for calcitic foraminifera<sup>40</sup>.

The compositional information derived from APT analysis of nacre tablet and mineral-organic interface associated with the interlamellar sheet were correlated with Photo-induced Force Microscopy (PiFM). PiFM is an emerging, sub-nanoscale AFM-based technique that allows for the simultaneous acquisition of 3D topographic data with spatially resolved molecular chemical information<sup>41</sup> and was used here to produce phase distribution maps at a spatial resolution similar to that of the APT reconstructions, but at a larger field of view that provides for more context of the sample. Figure 5a shows a 1 x 1  $\mu\text{m}$  topographic AFM map where three nacre tablets, separated by organic sheets (dark traces), meet. The characteristic nanogranular texture of nacre with granule sizes ranging between 15 to 55 nm ( $n = 30$ ) are in agreement with previous studies<sup>30,31,33</sup>. For the three PiFM phase distribution maps (Figs. 5b-d) obtained simultaneously with the topography map, aragonite was mapped using the characteristic band at  $1470\text{ cm}^{-1}$  (Fig. 5b, e<sup>42</sup>). Strontianite (Fig. 5c, e; green) was mapped via its peak associated with the asymmetric stretching mode that was visible as a small shoulder on one side of the aragonite band (Supplementary Fig. 9) at  $1444\text{ cm}^{-1}$ <sup>42</sup>. The proteinaceous organic moiety was mapped using the amide-I band at  $1658\text{ cm}^{-1}$ <sup>43</sup>, shown in red (Fig. 5d, e, Supplementary Fig. 9). The individual data channels shown in Fig. 5b to d, were combined into the PiFM composite map (Fig. 6a). This presentation of the data allows for the observation of phases that dominate certain subregions of the sample, while mixed colours highlight areas of co-located phases. For example, the organic interlamellar sheet between the nacre tablets is dominated by the organic moiety (red). Further, high intensities for strontianite (green) are clearly seen to be enriched adjacent to the organic interlamellar sheet and particularly in the cortices of nanogranules in this region. Throughout the map, most mineralized nanogranules contain Sr-rich and Sr-poor aragonite occurring separately, but spatially closely associated. Transects of the strontianite phase across individual nanogranules in different areas of the nacre tablets show a systematic pattern of nanogranules consisting of Sr-poorer aragonite cores outlined by 4 to 8 nm thick cortices of Sr-rich aragonite and strontianite towards their contours (Fig. 6b-e), which is in good agreement with the APT results. The transect of the nanogranule directly adjacent to the interlamellar sheet (Fig. 6b) confirms our

earlier observation that cortices in this area of the map are more enriched in Sr than those of other granules further inside the tablet (Fig. 6c-e).

## Discussion

Strontium pulse-chase labelling of bivalve shells produces timed 'snapshots' of different stages of nacre growth, which yield the first direct evidence for a two-step growth process of nacre that has been inferred as early as in the 1960's<sup>26</sup>: Extensional nacre growth occurs along the local growth direction of the shell normal to the organic interlamellar sheets (Fig. 2c, white arrows) and is complemented by space-filling growth of nacre tablets parallel to the interlamellar sheets (Fig. 2c, grey arrows). NanoSIMS maps of the labelled nacre (Fig. 2 Supplementary Fig. 2) indicate that extensional growth of nacre lamellae occurs simultaneously at multiple growth centres along the organic interlamellar sheet, forming the tablet centres of new nacre tablets. This observation supports literature studies indicating that extensional growth proceeds via mineral bridges via pores in the organic interlamellar sheets<sup>34,35</sup> often associated with screw dislocation<sup>28</sup>. The interplay of both modes of growth result in a stepped pattern of adjacent Sr-rich (i.e. labelled) and Sr-poor (i.e., unlabelled portions in the same nacre tablet) when shells are studied in cross-section (Fig. 2b and Supplementary Fig. 2, supplementary video).

Individual aragonitic nanogranules, the basic structural units of nacre tablets, are systematically zoned in Sr concentration at nanometre resolution: They display distinct Sr-enriched cortices towards the contours of the nanogranules and Sr-poor central parts. Sr-enrichments are clearly identified through significantly higher counts in the APT analyses (Figs. 3, 4, Supplementary Figs. 5 to 8) and through the presence and intensity of a shoulder indicative for strontianite in the PiFM spectra (Figs. 5, 6). At tablet-scale, nanogranules along the rim of a nacre tablet (Fig. 6a) adjacent to the organic sheet are more enriched in Sr compared to other areas in the nacre tablets.

Cortices of similar dimensions in nacre, including in nacre nanogranules have been previously reported in the literature, however, these structures were only identified by phase composition (i.e., presence or absence of ACC) and not, as presented here, based on their chemical composition: Nassif et al.<sup>12</sup> reported similarly sized, 3–5 nm thick ACC layers coating the nacre tablets in *Haliothis laevigata*. In the shell of *Phorcus turbinatus* and at spatial resolution of individual nanogranules, Macias-Sanchez et al.<sup>33</sup> observed 5–10 nm thick ACC cortices coating crystalline aragonite nanogranules (referred to as 'nanoglobules'). Both studies<sup>12,33</sup> argue that these ACC cortices represent vestiges of the non-classical crystallisation pathway of nacre and are stabilized by trace metal ions and/or organic molecules expelled from ACC upon crystallization of aragonite.

Similarly, we interpret the Sr cortices observed here as a result of phase transformation of ACC to aragonite, created by the exclusion of excess Sr upon crystallization of aragonite. Hence, in these initial stages of crystallization each organic-coated nanogranule<sup>30,44,45</sup> serves as a compartment for the ACC to aragonite transformation<sup>33</sup>. Laboratory studies have shown that the dehydration of ACC serves as an

effective trigger for crystallisation<sup>46</sup> and it has been suggested that the presence of these small amounts of surface water mediate the formation of the crystalline phase by dissolution and reprecipitation<sup>2,46</sup>. For the first time here, we provide evidence in naturally formed nacre through the formation of Sr-rich cortices in nanogranules, that the ACC-to-aragonite transformation proceeds via an intragranular and spatially-confined dissolution-reprecipitation mechanism that preserves the fine structure of the material<sup>47</sup>.

Exposed to Sr-enriched seawater, excess amounts of strontium are non-selectively incorporated in the growing shell due to the lack of long-range order of the ACC structure<sup>16,48-50</sup>. Upon crystallization, the formation of aragonite is energetically favoured over strontianite<sup>51</sup>, although both are isostructural<sup>52,53</sup>. Thus, excess strontium is excluded from the aragonite lattice and forms Sr-rich CaCO<sub>3</sub> cortices along the outer contours of the nanogranules. Since Sr ions can stabilize ACC<sup>54</sup> these cortices are most likely amorphous when they form and may remain so for extended periods of time.

The systematic presence of strontium-enriched cortices and Sr-poor cores in individual nanogranules throughout the nacre tablet indicates that the major transformation mechanism is the dissolution of the ACC structure to crystallize the CaCO<sub>3</sub> as aragonite. Aragonite has a different strontium content governed by its selective crystal chemistry<sup>55</sup> and therefore leads to Sr-enriched cortices, while transformation via solid-state mechanisms would not affect the chemical composition. Such very localized dissolution and reprecipitation processes successfully preserve the nanogranular texture of nacre.

Spatially coupled dissolution-reprecipitation reactions that preserve the fine structures and overall shape of the replaced mineral, kinetically outcompete solid-state transformation reactions and are, in fact, very common in mineralized systems<sup>56</sup>. They are catalysed by a fluid and are usually driven by small free energy differences between the reaction partner phases. Specifically, in interface-coupled systems with an interfacial fluid<sup>47</sup>, the dissolution rate of one and the activation energy barrier for nucleation of the other reaction partner create local equilibrium conditions which result in the preservation of very fine structural details after phase transformation<sup>57,58</sup>.

A common issue encountered in laboratory dissolution-reprecipitation experiments is the significant morphological change occurring during transformation<sup>15,16</sup> which fail to explain the preservation of the hierarchical ultrastructure observed in natural biominerals and, hence, seem to support solid state transformation of ACC to the crystalline calcium carbonate phase. Our findings here solve this long-standing question and show that in natural nacre, the fine structural details of the material are preserved due to a spatially coupled dissolution-reprecipitation mechanism that takes place in nanogranular compartments delineated by organic coatings.

## Methods

### Aquaculture

Juvenile Mediterranean mussels *Mytilus galloprovincialis* (Lamarck, 1819) were collected alive from Twofold Bay, New South Wales, Australia and brought to the Macquarie University Seawater Facility. About 50 juvenile mussels sized 5 to 30 mm were evenly divided into two 50 L polyethylene tanks that were connected to a recirculating system for sterilized, filtered natural seawater sourced outside the Sydney harbour. The tanks were maintained at local ocean temperature, salinity and pH, while the lighting was adjusted to a circadian day/night cycle. The mussels were fed daily using a microalgae mix and maintained according to previously published protocols<sup>21,29</sup>. After 3 weeks of acclimatization, the experimental period consisted of 35 to 55 days in which bivalves were transferred 4 times (group 1) and 3 times (group 2) from ambient seawater (8 µg/g Sr at salinity of 35 psu) to conditions with elevated Sr concentrations of 120 µg/g (15x mean ocean water). The Sr-enriched seawater was produced by dissolving 0.37 g SrCl<sub>2</sub>•6H<sub>2</sub>O/litre seawater into the tanks. Sr labelling intervals were maintained for 3 (group 1) and 6 (group 2) days and enriched seawater was fully replaced every 48 h. Between the labelling events, mussels were transferred back to ambient conditions for 6 (group 1) and 12 (group 2) days. After the last labelling event mussels were collected and deep-frozen at -20°C. After the experiments, soft tissues were removed, shells were rinsed in deionized water and air-dried.

**Sample preparation.** Shells were mounted in EpoFix epoxy resin (Struers, Australia) and left to cure in the fridge at 2°C. Lapping and polishing followed protocols published previously<sup>21,59</sup> and consisted of a series of 500 to 4000 grit diamond lapping discs, followed by 3 and 1 µm diamond suspensions and a diluted suspension of 0.25 µm colloidal silica concluded the polishing. Polished mounts were used for PiFM without any additional preparation steps, while SEM-EDS and NanoSIMS analyses required sputter coating with carbon (20 nm) and gold (10 nm), respectively.

Specimens for APT were prepared using the Xe beam of a ThermoFisher Helios Hydra G4 UXe DualBeam Plasma Focussed Ion Beam-Scanning Electron Microscope (FIB-SEM) at the Australian Centre for Microscopy and Microanalysis (ACMM), University of Sydney. Regions of interest in the shells were BSE imaged to clearly visualize the Sr labelled nacre layers to accurately depositing the platinum protection strips onto the target areas for liftout (Supplementary Fig. 3). This approach also avoided direct S/TEM imaging of the APT tips after milling, which can cause damage to the structure of the biomineral architecture, thus increasing the risk of fracturing during the APT run<sup>29</sup>. *In situ* liftouts were performed by using an accelerating voltage of 30 kV and a beam current of 1 nA. Annular milling was performed using a Zeiss Auriga FIB-SEM starting at 30 kV and 1 nA and stepping down the voltage and current to 10 kV and 50 pA. As nacre is a highly beam-sensitive material, it was crucial to use suitable FIB parameters and to maintain adequately low (i.e., < 2 kV) electron-beam conditions for imaging during preparation<sup>29</sup>.

**Scanning Electron Microscopy-Energy Dispersive X-Ray Spectroscopy (SEM-EDS).** A Zeiss EVO MA15 tungsten SEM equipped with an Oxford 20 mm<sup>2</sup> X-max SDD EDS detector at Macquarie University was used to obtain Z-sensitive BSE images and quantitative SEM-EDS maps of Sr-labelled nacre. BSE images were obtained at 15 kV and 10 nA. SEM-EDS mapping was carried out in high vacuum using the AZtec acquisition software (version 3.1) and operating conditions were 20 kV accelerating voltage, 12 mm

working distance and 200 pA beam current. The primary electron beam was focused to a spot size of 400 nm that scanned a map area of 80 x 60  $\mu\text{m}$  at a resolution of 1,027 x 768 pixels. A ZAF correction was applied automatically by the software and major element concentrations resemble previous wavelength dispersive analysis<sup>21</sup>.

**Nanoscale Secondary Ion Mass Spectrometry (NanoSIMS).**  $^{88}\text{Sr}/^{40}\text{Ca}$  isotope abundances were mapped using a new generation CAMECA NanoSIMS 50 L ion probe at the University of Western Australia. Operation conditions followed procedures published previously<sup>21</sup>. A Hyperion RF plasma oxygen ion source produced a primary oxygen ion beam that was focused to a spot size of 100 nm to scan 50 x 50  $\mu\text{m}$  map areas at a resolution of 512 x 512 pixels<sup>2</sup>. Both Ca and Sr isotopes were measured on electron multipliers at 5000 mass resolution.

**Atom Probe Tomography (APT).** APT experiments were carried out on a CAMECA LEAP 4000Si at the ACMM, University of Sydney. This system is equipped with an ultraviolet laser that produces picosecond-pulses at an excitation wavelength of 355 nm. Operating parameters followed the protocol in Eder et al.<sup>29</sup> and consisted of a pulse energy of 100–200 pJ, a pulse frequency of 160 kHz and a 0.5% detection rate yielded a data set of 3 million detector hits (Supplementary Fig. 4). During analysis, the sample was cooled to 50 K in ultrahigh vacuum ( $< 2 \cdot 10^{-11}$  Pa). The tip shape geometries of all datasets were calibrated by using SEM images, which gives a more accurate result for biominerals than using the voltage evolution curve<sup>29</sup>. Then, data reconstruction, 3D visualization and compositional profiles were obtained using IVAS v3.8.4 software. All compositional profiles (i.e., proxigrams, Fig. 4, Supplementary Figs. 6 and 8) were prepared from a cylindrical region (e.g., sized 48 x 48 x 31 nm in Fig. 4) traversing the APT data sub-sets. These compositional profiles provide a valuable, qualitative guide for the local distributions of specific element species. However, the uneven mineral-organic interface as well as trajectory aberrations caused by the difference in evaporation fields between the calcium carbonate and the organic matrices can lead to deviations their thickness and composition in the reconstructed data<sup>29,60</sup>. Hence, the APT data of this study are only qualitative. For a full list of all the ion species detected see Table S1 in Eder et al.<sup>29</sup>. We divide the line data shown in the compositional profiles into three sections referred to as 'tablet', 'cortex' and 'interlamellar sheet' (black dashed lines): The dashed line marking the tablet-cortex transition, was defined by the significant, abrupt increase in Sr, while the dashed line marking the cortex-interlamellar sheet transition, was set to the intercept point of Ca and C lines (Fig. 4, Supplementary Figs. 6 and 8).

**Photo-induced Force Microscopy (PiFM).** PiFM analyses was carried out using a commercial VistaScope microscope at Molecular Vista Inc. San Jose, CA-USA. We used a quantum cascade laser (QCL)-module from Block Engineering LLC as excitation source. This laser module consists of four serially connected gap-free QCLs that provide access to a wide wavenumber range of 770 to 1860  $\text{cm}^{-1}$ . Measurements were conducted in dynamic AC AFM mode using a Nanosensors™ 300 kHz platinum iridium-coated, non-contact, silicon-based AFM probe (NanoWorld AG, Switzerland). For more details on the instrumentation and methodology see Otter et al.<sup>41</sup>.

The strontianite is identified by a band at  $1444\text{ cm}^{-1}$  which is characteristic for the asymmetric stretching modes ( $n_1$ )<sup>42</sup>. This peak is only visible within the Sr labelled shell portions as a small shoulder to one side of the larger aragonite peak (asymmetric stretching mode  $n_1$ ) at  $1470\text{ cm}^{-1}$ <sup>42</sup> and was absent in unlabelled shell portions. We conclude here that strontianite is only present in nano-domains within an aragonite-rich crystallographic environment. The proteinaceous organic moiety of the shell was mapped using the amide-I band at  $1658\text{ cm}^{-1}$ <sup>43</sup>.

## Declarations

## Data availability

All relevant data supporting the findings of this study are available from the corresponding author upon request.

## Acknowledgements

We thank Eden Mussels for providing *M. galloprovincialis*. We acknowledge Assoc. Prof Jane Williamson and Josh Aldridge for assistance at the Macquarie Seawater Facility and we are grateful to Dr Wayne O'Connor (Port Stephens Fisheries Centre, NSW Department of Primary Industries) for insightful discussions on bivalve aquaculture. Further, we thank Dr Paul Guagliardo for his assistance with NanoSIMS analysis and Dr Sean Murray for his assistance with SEM imaging, Dr Timothy D. Murphy for assistance with quantitative SEM-EDS mapping and Dr Oscar Branson for discussions on APT data. The authors are grateful for the scientific and technical input and support from Microscopy Australia at the University of Sydney and the University of Western Australia. This study is supported by the Australian Research Council (DP160102081 and DP210101268) to DEJ and a Beate Mocek Price awarded through the German Mineralogical Society awarded to LMO.

## Author contributions

LMO and DEJ designed the study. LMO performed aquaculture experiments, prepared samples and participated in data collection. KE and JMC conducted atom probe experiments. LY prepared APT tips. MRK performed NanoSIMS analysis. DBN and PO'R performed PiFM analysis. LMO wrote the first draft of the manuscript with contributions from all co-authors.

## Competing Financial Interests.

The authors declare no competing financial interests.

## References

1. Addadi, L., Raz, S. & Weiner, S. Taking advantage of disorder. Amorphous calcium carbonate and its roles in biomineralization. *Advanced Materials* **15**, 959–970 (2003).
2. De Yoreo, J. J. *et al.* Crystallization by particle attachment in synthetic, biogenic, and geologic environments. *Science* **349**, 1–9 (2015).
3. Politi, Y. *et al.* Transformation mechanism of amorphous calcium carbonate into calcite in the sea urchin larval spicule. *Proceedings of the National Academy of Sciences* **105**, 17362–17366 (2008).
4. Jacob, D. E., Wirth, R., Soldati, A. L., Wehrmeister, U. & Schreiber, A. Amorphous calcium carbonate in the shells of adult Unionoida. *Journal of Structural Biology* **173**, 241–249 (2011).
5. Weiss, I. M., Tuross, N., Addadi, L. & Weiner, S. Mollusc larval shell formation. Amorphous calcium carbonate is a precursor phase for aragonite. *Journal of Experimental Zoology* **293**, 478–491 (2002).
6. Cölfen, H. & Mann, S. Higher-order organization by mesoscale self-assembly and transformation of hybrid nanostructures. *Angewandte Chemie International Edition* **42**, 2350–2365 (2003).
7. Li, D. *et al.* Direction-specific interactions control crystal growth by oriented attachment. *Science* **336**, 1014–1018 (2012).
8. Schöne, B. R. & Gillikin, D. P. *Unraveling environmental histories from skeletal diaries—advances in sclerochronology* (Elsevier, 2013).
9. Prendergast, A. L. *et al.* Oxygen isotopes from *Phorcus* (*Osilinus*) *turbinatus* shells as a proxy for sea surface temperature in the central Mediterranean. A case study from Malta. *Chemical Geology* **345**, 77–86 (2013).
10. Versteegh, E. A. A. *et al.* Oxygen isotope ratios in the shell of *Mytilus edulis*. Archives of glacier meltwater in Greenland? *Biogeosciences* **9**, 5231–5241 (2012).
11. Gaetani, G. A. & Cohen, A. L. Element partitioning during precipitation of aragonite from seawater. A framework for understanding paleoproxies. *Geochimica et Cosmochimica Acta* **70**, 4617–4634 (2006).
12. Nassif, N. *et al.* Amorphous layer around aragonite platelets in nacre. *Proceedings of the National Academy of Sciences of the United States of America* **102**, 12653–12655 (2005).
13. Raiteri, P. & Gale, J. D. Water is the key to nonclassical nucleation of amorphous calcium carbonate. *Journal of the American Chemical Society* **132**, 17623–17634 (2010).
14. Liu, Z. *et al.* Shape-preserving amorphous-to-crystalline transformation of CaCO<sub>3</sub> revealed by in situ TEM. *Proceedings of the National Academy of Sciences* **117**, 3397–3404 (2020).
15. Blue, C. R. *et al.* Chemical and physical controls on the transformation of amorphous calcium carbonate into crystalline CaCO<sub>3</sub> polymorphs. *Geochimica et Cosmochimica Acta* **196**, 179–196 (2017).
16. Littlewood, J. L. *et al.* Mechanism of enhanced strontium uptake into calcite via an amorphous calcium carbonate crystallization pathway. *Crystal Growth & Design* **17**, 1214–1223 (2017).

17. Navrotsky, A. Energetic clues to pathways to biomineralization. Precursors, clusters, and nanoparticles. *Proceedings of the National Academy of Sciences* **101**, 12096–12101 (2004).
18. Giuffrè, A. J., Gagnon, A. C., Yoreo, J. J. de & Dove, P. M. Isotopic tracer evidence for the amorphous calcium carbonate to calcite transformation by dissolution–reprecipitation. *Geochimica et Cosmochimica Acta* **165**, 407–417 (2015).
19. Jacob, D. E., Wirth, R., Agbaje, O. B.A., Branson, O. & Eggins, S. M. Planktic foraminifera form their shells via metastable carbonate phases. *Nature Communications* **8**, 1–9 (2017).
20. DeVol, R. T. *et al.* Nanoscale transforming mineral phases in fresh nacre. *Journal of the American Chemical Society* **137**, 13325–13333 (2015).
21. Otter, L. M. *et al.* Insights into architecture, growth dynamics, and biomineralization from pulsed Sr-labelled *Katelysia rhytiphora* shells (Mollusca, Bivalvia). *Biogeosciences* **16**, 3439–3455 (2019).
22. Houlbrèque, F. *et al.* Strontium-86 labeling experiments show spatially heterogeneous skeletal formation in the scleractinian coral *Porites porites*. *Geophysical Research Letters* **36** (2009).
23. Gorzelak, P., Stolarski, J., Dubois, P., Kopp, C. & Meibom, A. 26 Mg labeling of the sea urchin regenerating spine: Insights into echinoderm biomineralization process. *Journal of Structural Biology* **176**, 119–126 (2011).
24. Brahmi, C. *et al.* Pulsed <sup>86</sup>Sr-labeling and NanoSIMS imaging to study coral biomineralization at ultra-structural length scales. *Coral Reefs* **31**, 741–752 (2012).
25. Gim, J. *et al.* Nanoscale deformation mechanics reveal resilience in nacre of *Pinna nobilis* shell. *Nature Communications* **10**, 1–8 (2019).
26. Bevelander, G. & Nakahara, H. An electron microscope study of the formation of the nacreous layer in the shell of certain bivalve molluscs. *Calcified Tissue Research* **3**, 84–92 (1969).
27. Weiner, S., Traub, W. & Parker, S. B. Macromolecules in mollusc shells and their functions in biomineralization [and Discussion]. *Philosophical Transactions of the Royal Society of London B: Biological Sciences* **304**, 425–434 (1984).
28. Gim, J. *et al.* The mesoscale order of nacreous pearls. *Proceedings of the National Academy of Sciences* **118** (2021).
29. Eder, K., Otter, L. M., Yang, L., Jacob, D. E. & Cairney, J. M. Overcoming Challenges Associated with the Analysis of Nacre by Atom Probe Tomography. *Geostandards and Geoanalytical Research* **43**, 385–395 (2019).
30. Jacob, D. E. *et al.* Nanostructure, composition and mechanisms of bivalve shell growth. *Geochimica et Cosmochimica Acta* **72**, 5401–5415 (2008).
31. Hovden, R. *et al.* Nanoscale assembly processes revealed in the nacreprismatic transition zone of *Pinna nobilis* mollusc shells. *Nature Communications* **6**, 1–7 (2015).
32. Checa, A. G. *et al.* Crystallographic control on the substructure of nacre tablets. *Journal of Structural Biology* **183**, 368–376 (2013).

33. Macías-Sánchez, E., Willinger, M. G., Pina, C. M. & Checa, A. G. Transformation of ACC into aragonite and the origin of the nanogranular structure of nacre. *Scientific Reports* **7**, 1–11 (2017).
34. Checa, A. G., Cartwright, J. H. E. & Willinger, M.-G. Mineral bridges in nacre. *Journal of Structural Biology* **176**, 330–339 (2011).
35. Olson, I. C. *et al.* Crystal nucleation and near-epitaxial growth in nacre. *Journal of Structural Biology* **184**, 454–463 (2013).
36. Schäffer, T. E. *et al.* Does abalone nacre form by heteroepitaxial nucleation or by growth through mineral bridges? *Chemistry of Materials* **9**, 1731–1740 (1997).
37. Lin, A. Y.-M., Chen, P.-Y. & Meyers, M. A. The growth of nacre in the abalone shell. *Acta Biomaterialia* **4**, 131–138 (2008).
38. Cohen, A. L. & McConnaughey, T. A. Geochemical perspectives on coral mineralization. *Reviews in Mineralogy and Geochemistry* **54**, 151–187 (2003).
39. Nakahara, H. & Bevelander, G. The formation and growth of the prismatic layer of *Pinctada radiata*. *Calcified Tissue Research* **7**, 31–45 (1971).
40. Branson, O. *et al.* Nanometer-scale chemistry of a calcite biomineralization template. Implications for skeletal composition and nucleation. *Proceedings of the National Academy of Sciences* **113**, 12934–12939 (2016).
41. Otter, L. M. *et al.* Nanoscale Chemical Imaging by Photo-Induced Force Microscopy. Technical Aspects and Application to the Geosciences. *Geostandards and Geoanalytical Research* **45**, 5–27 (2021).
42. Wang, X. *et al.* High-temperature Raman and FTIR study of aragonite-group carbonates. *Physics and Chemistry of Minerals* **46**, 51–62 (2019).
43. Parker, F. S. Amides and amines. In *Applications of infrared spectroscopy in biochemistry, biology, and medicine* (Springer 1971), pp. 165–172.
44. Rousseau, M. *et al.* Multiscale structure of sheet nacre. *Biomaterials* **26**, 6254–6262 (2005).
45. Wolf, S. E. *et al.* Merging models of biomineralisation with concepts of nonclassical crystallisation. Is a liquid amorphous precursor involved in the formation of the prismatic layer of the Mediterranean Fan Mussel *Pinna nobilis*? *Faraday Discussions* **159**, 433–448 (2012).
46. Ihli, J. *et al.* Dehydration and crystallization of amorphous calcium carbonate in solution and in air. *Nature Communications* **5**, 1–10 (2014).
47. Putnis, A. Why mineral interfaces matter. *Science* **343**, 1441–1442 (2014).
48. Clark, S. M. *et al.* The nano-and meso-scale structure of amorphous calcium carbonate. *Scientific Reports* **12**, 1–12 (2022).
49. Gebauer, D. & Wolf, S. E. Designing solid materials from their solute state. A shift in paradigms toward a holistic approach in functional materials chemistry. *Journal of the American Chemical Society* **141**, 4490–4504 (2019).

50. Gilbert, P. U. *et al.* Biomineralization. Integrating mechanism and evolutionary history. *Science Advances* **8**, eabl9653 (2022).
51. Robie, R. A. Thermodynamic properties of minerals and related substances at 298.15 K and 1 bar (105 Pascal) pressure and at higher temperatures. *US Geol. Surv. Bull.* **1452**, 298–310 (1978).
52. De Villiers, J.P.R. The Crystal Structures of Aragonite, Strontianite, and Witherite. *American Mineralogist* **56**, 758–767 (1971).
53. Finch, A. A. & Allison, N. Coordination of Sr and Mg in calcite and aragonite. *Mineralogical Magazine* **71**, 539–552 (2007).
54. Schmidt, I. *et al.* Effect of strontium ions on crystallization of amorphous calcium carbonate. *Crystal Research and Technology* **54**, 1900002 (2019).
55. Plummer, L. N. & Busenberg, E. Thermodynamics of aragonite-strontianite solid solutions. Results from stoichiometric solubility at 25 and 76 C. *Geochimica et Cosmochimica Acta* **51**, 1393–1411 (1987).
56. Putnis, A., Oelkers, E. H. & Schott, J. Mineral replacement reactions. Thermodynamics and kinetics of water-rock interaction **70**, 87–124 (2009).
57. Álvarez-Lloret, P., Rodríguez-Navarro, A. B., Falini, G., Fermani, S. & Ortega-Huertas, M. Crystallographic control of the hydrothermal conversion of calcitic sea urchin spine (*Paracentrotus lividus*) into apatite. *Crystal Growth & Design* **10**, 5227–5232 (2010).
58. Xia, F. *et al.* Three-Dimensional ordered arrays of zeolite nanocrystals with uniform size and orientation by a pseudomorphic coupled dissolution – reprecipitation replacement route. *Crystal Growth & Design* **9**, 4902–4906 (2009).
59. Jacob, D. E. *et al.* Architecture and biomineralization of *Anoteropora latirostris* (Bryozoa, Cheilostomata). *Scientific Reports* **9**, 1–13 (2019).
60. Cappelli, C., Smart, S., Stowell, H. & Pérez-Huerta, A. Exploring biases in atom probe tomography compositional analysis of minerals. *Geostandards and Geoanalytical Research* **45**, 457–476 (2021).

## Figures

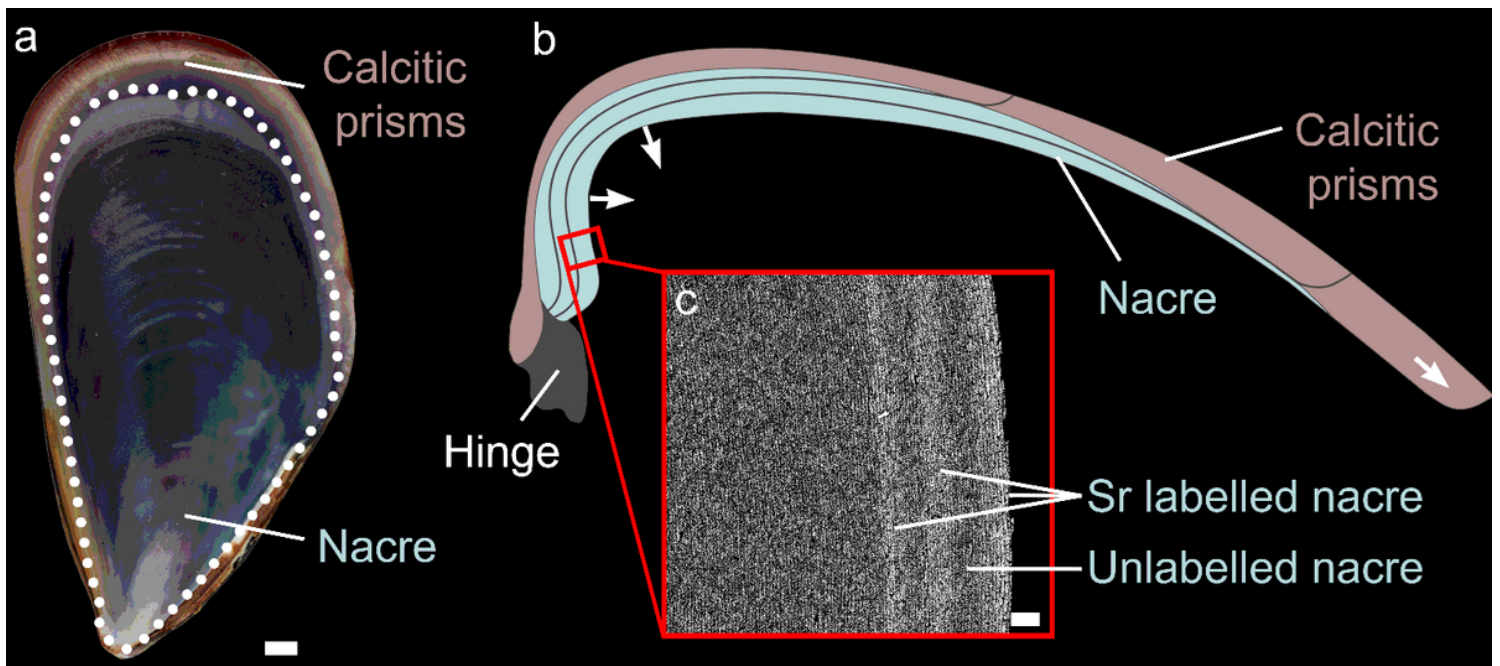


**Figure 1**

Nacre growth visualized by Sr pulse-chase labelling. **a** Image of the inner shell surface of a *M. galloprovincialis* shell showing nacre constituting most of the inner shell surface inside the white dotted line and prismatic calcite outside the line. **b** schematic cross-section of a shell. The shell grows in length by extending the outer calcitic layer along the ventral margin (white arrow). The inner nacreous shell layer extends by thickening the inner shell surface (two white arrows). **c** SEM-BSE image (inset in b) of a polished shell cross-section showing Sr-labelled nacre layers as three light grey bands tracing parallel to the inner shell edge, while shell portions grown in normal seawater composition are shown in darker grey. In this region, the nacre layer grew 25  $\mu\text{m}$  over the experimental period of 46 days marked by the start of the innermost Sr label. Scale bars are 1 mm (a) and 5  $\mu\text{m}$  (b inset).

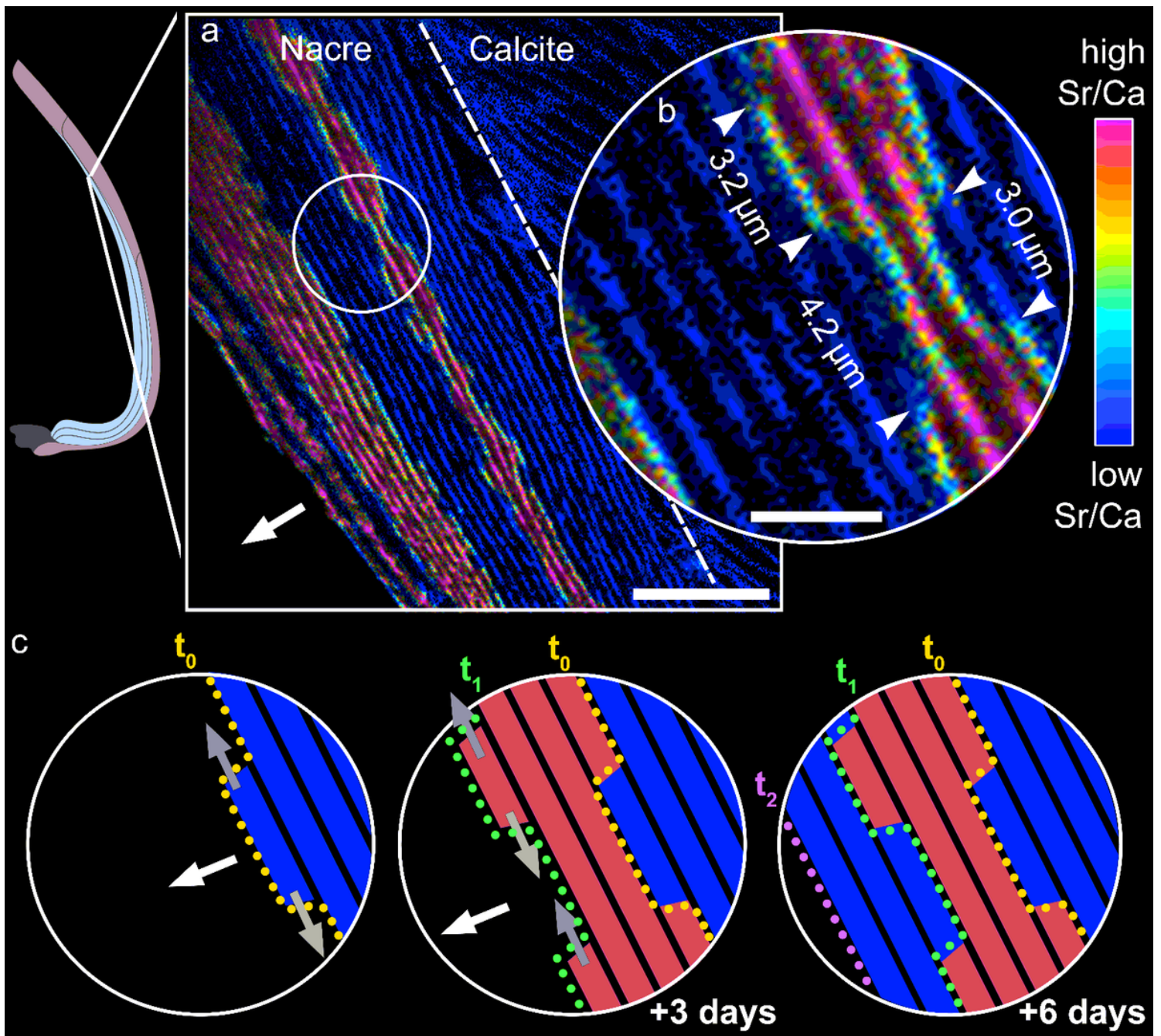


**Figure 2**

NanoSIMS imaging of dynamic nacre growth processes visualised via Sr pulse chase labelling. **a**  $^{88}\text{Sr}/^{40}\text{Ca}$  ratio map sized 50 x 50 μm showing four Sr labels (magenta) and unlabelled nacre (blue) in a hue–saturation–intensity (HSI) colour scale parallel to the nacre growth front. The combined unlabelled and labelled nacre layers have average Sr concentrations of 2,100 μg/g and 12,500 μg/g, respectively (Supplementary Table 2). The labelled nacre layers exhibit a stepped growth pattern of intercalated nacre tablets formed in seawater with normal Sr concentration (blue) and during Sr-labelling (magenta). **b** Magnified region of interest (circled in a) shows sharp (i.e., within 100 nm) near-vertical transitions, marked by white arrowheads, between labelled and unlabelled portions of nacre lamellae. The sizes of neighbouring labelled and unlabelled lamellae portions ranging between 3.0 to 4.2 μm indicate that these

portions represent changes in Sr/Ca ratios within individual tablets as the total tablet length of a nacre tablet is 10-20  $\mu\text{m}$ . **c** Time-resolved schematic representation of the two components of nacre growth processes (area corresponds to that shown in b): extensional nacre growth across layers normal to the organic interlamellar sheets (white arrows) and space-filling nacre growth of individual tablets parallel with the interlamellar sheet within individual nacre layers (grey arrows). Growth between  $t_0$  (yellow dotted line) and  $t_1$  (green dotted line) was achieved within 3 days and nacre lamellae between  $t_1$  and  $t_2$  (purple dotted line) formed within the following 6 days (see Supplementary video for a full animation of the growth sequence). This time-resolved illustration of nacre growth demonstrates that extensional growth, thickening the shell is followed by space-filling growth of separate individual nacre tablets). For additional NanoSIMS maps see Supplementary Fig. 2. Scale bar is 10  $\mu\text{m}$  (a) and 3  $\mu\text{m}$  (b, c, d).

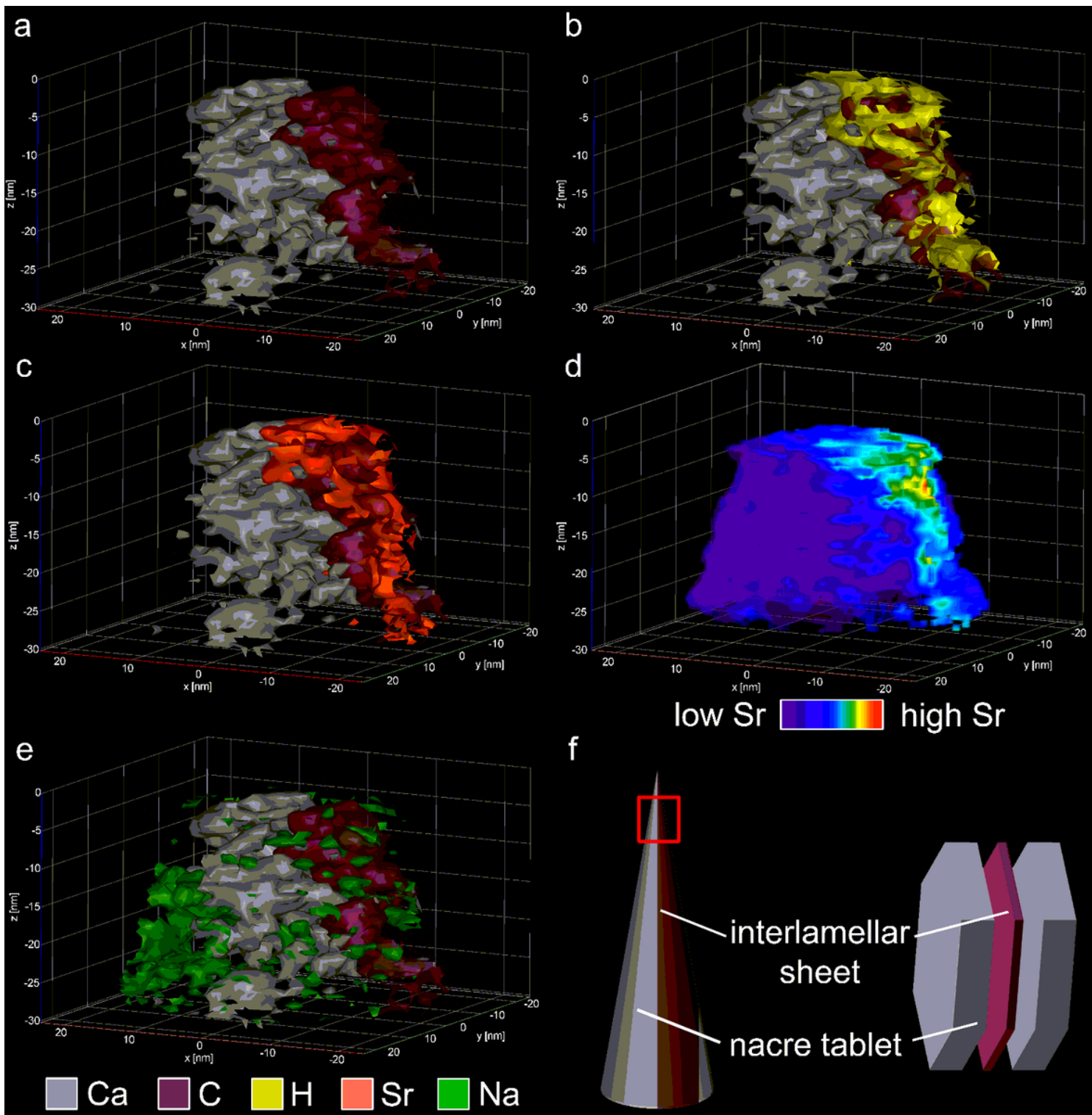


**Figure 3**

3D APT reconstruction of the nacre tablet and the mineral-organic interface associated with the interlamellar sheet in Sr-labelled nacre sized 50 nm x 50 nm x 30 nm. **a** iso-concentration surfaces of Ca (50 at%, grey) depicting the outer area of a nacre tablet and elevated C (5.1 at%, magenta) identifies the organic interlamellar sheet. **b** iso-concentration surfaces of H (10 at%, yellow) co-located with high C concentrations in the organic interlamellar sheet **c** the iso-concentration surface of Sr (20 at%, red) shows a distinctly enriched cortex within nacre adjacent to the organic sheet. **d** volume rendering, in a heat-map

colour scale, showing the distribution of Sr across the volume of the reconstruction highlighting the Sr enriched cortex (red to yellow) in the nacre tablet **e** iso-concentration surfaces of Na (8 at%, green) forms a distinct cluster within the mineral phase next to the Sr-rich cortex **f** schematic representation of the APT reconstruction (red box) and its relative position within the tip as well as within the nacreous architecture more generally.

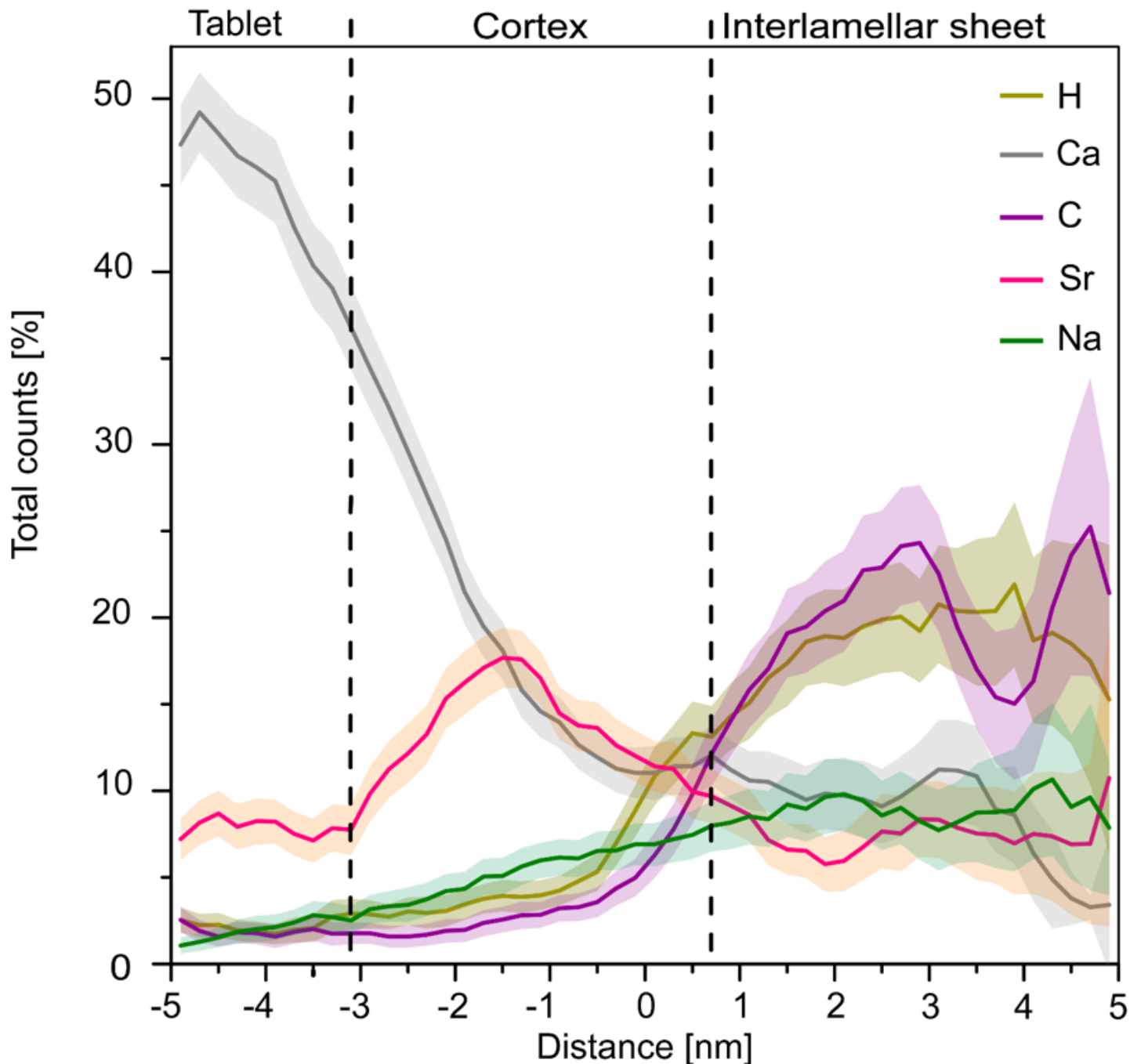


**Figure 4**

Qualitative compositional profile for the area shown in Fig. 3 across the nacre tablet and the mineral-organic interface associated with the interlamellar sheet. The profile is divided by black dashed lines into three sections 'tablet', 'cortex' and 'interlamellar sheet'. The tablet-cortex transition is defined by a

significant increase in Sr, while the transition from cortex to interlamellar sheet is defined as the point of intersection between the Ca (grey) and the C (magenta) signals (see methods). The 'tablet' is characterized by high Ca concentrations indicative of  $\text{CaCO}_3$ , while the 'cortex' area is defined by high Sr (red) at intermediate Ca and the 'interlamellar sheet' by high C and H (yellow) counts indicative of organics. The Sr-enriched cortex appears within 4 nm of the mineralized nacre tablet adjacent to the organic sheet. The abundance of Na (green) increases steadily from the tablet into the organic sheet. Shaded error envelopes are calculated based on counting statistics.

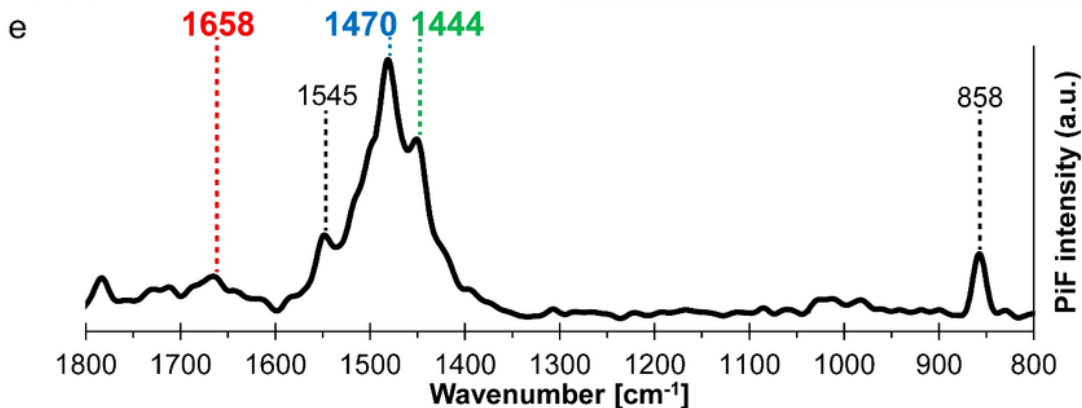
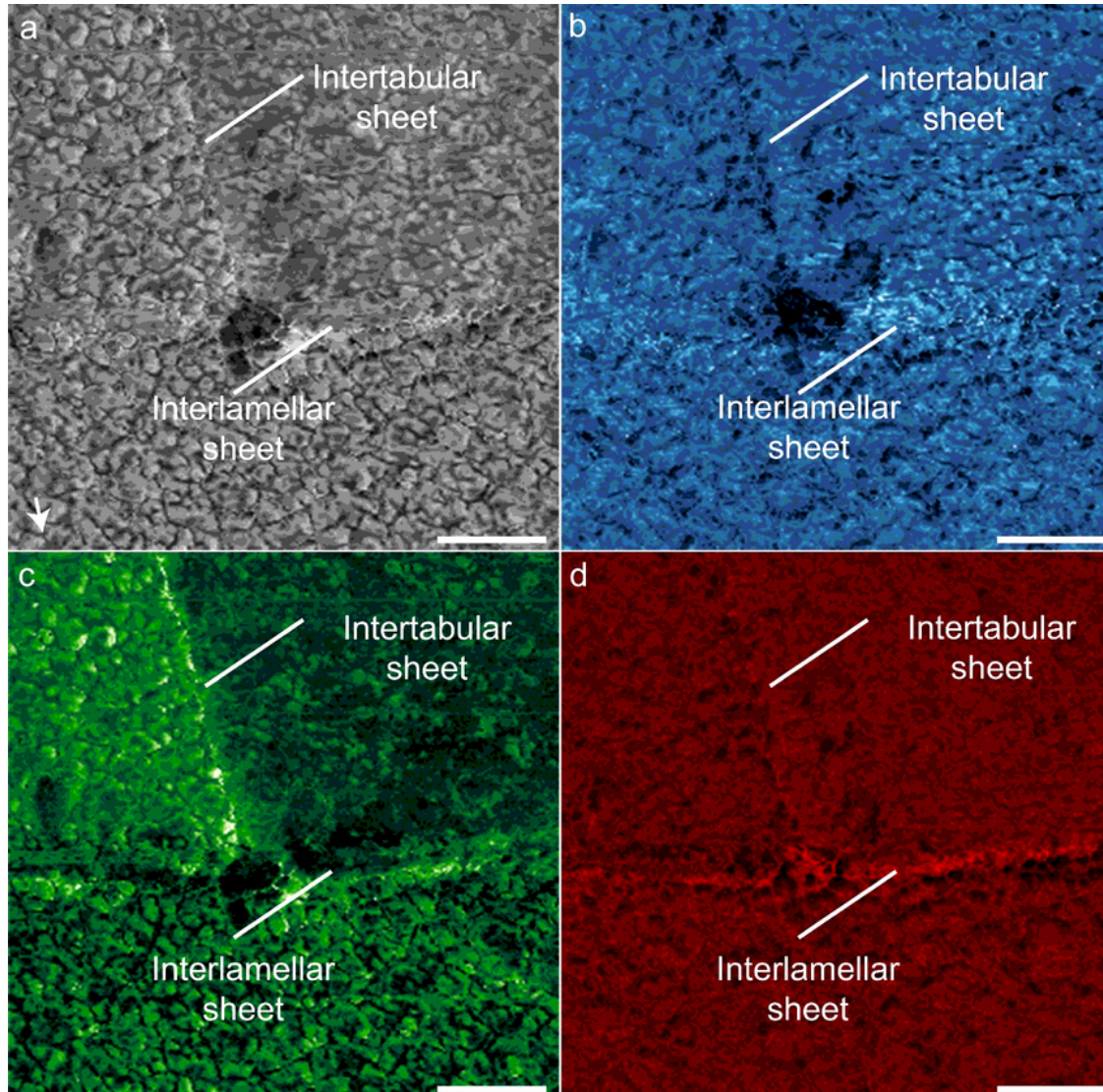


## Figure 5

Separate PiFM phase distribution maps across Sr-labelled nacre and the mineral-organic interfaces. **a** topographic AFM image sized 1 x 1  $\mu\text{m}$  with lighter and darker colour representing differences in topography (0-20 nm), the white arrow points towards the direction of extensional nacre growth **b** shows the distribution of aragonite mapped at  $1470\text{ cm}^{-1}$ , **c** strontianite mapped at  $1445\text{ cm}^{-1}$  and **d** phase distribution of the proteinaceous organic moiety was mapped using the amide-I band at  $1658\text{ cm}^{-1}$ . Aragonite is homogeneously distributed across the bulk of the tablets and decreases significantly at the organic sheets. Strontianite is enriched along the contours of individual nanogranules throughout the tablet and strongly enriched around nanogranules adjacent to the organic interlamellar sheet. All four maps were acquired simultaneously and have a pixel resolution of 4 nm. For a PiFM overview map see Supplementary Fig. 9. Scale bars are 200 nm.

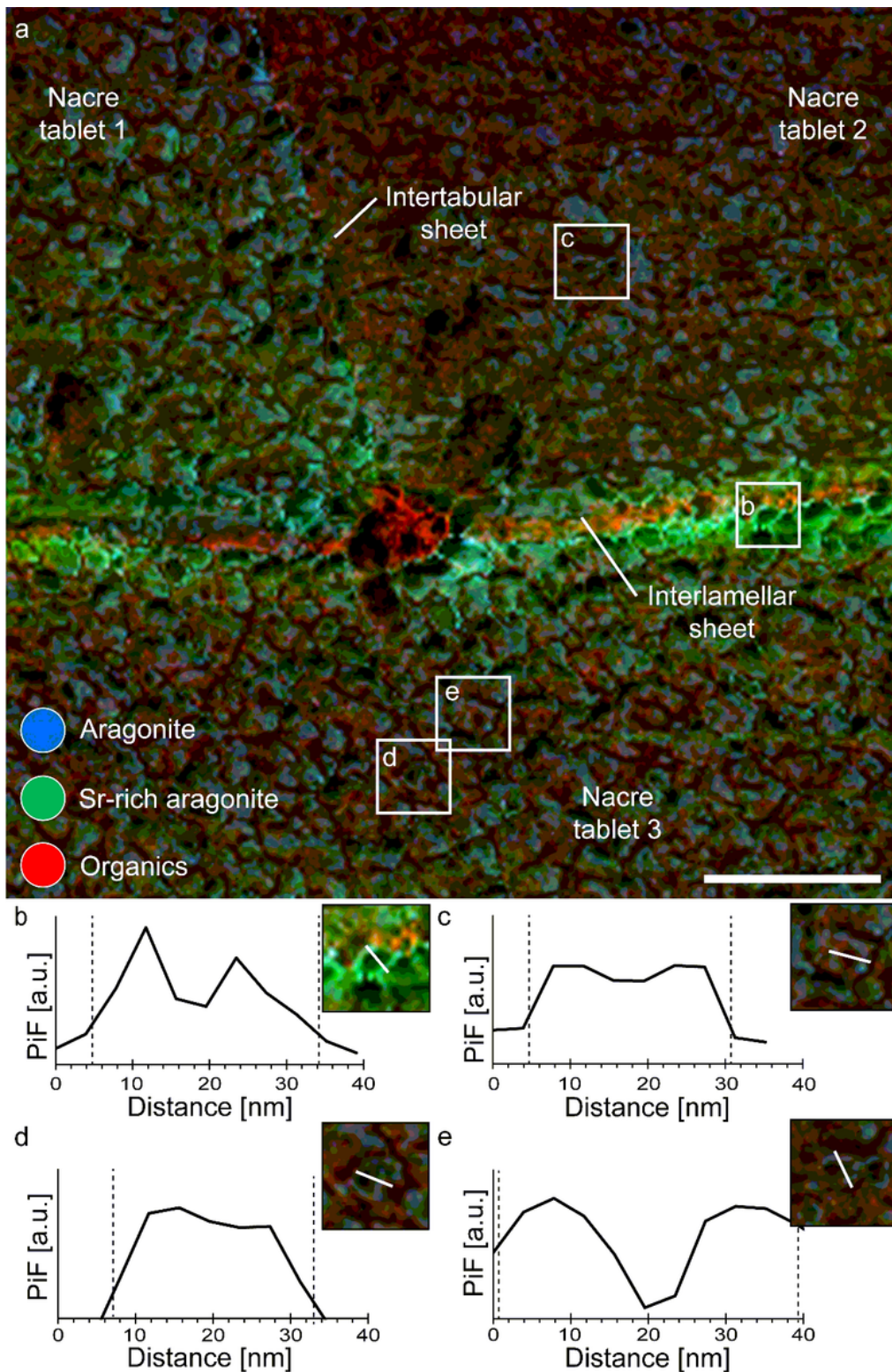


**Figure 6**

Spatial distribution of inorganic and organic phases across Sr-labelled nacre tablets. **a** PiFM map sized 1 x 1  $\mu\text{m}$ , showing the colour-coded data channels from Fig. 5 combined into one composite map. This mode of presentation allows to determine which phase dominates in certain subregions of the sample, while mixed colours highlight areas of co-located phases. **b** to **e** show a 40 nm long transects of the strontianite phase across individual nanogranules with the location highlighted by white boxes in **a**. The

nanogranule shown in **b** is located at the mineral-organic interface associated with the interlamellar sheet, while those shown in **c**, **d** and **e** are located further away from it. At tablet-scale, strontium-rich aragonite (green), is enriched at the outer nacre tablet periphery adjacent to the interlamellar sheet. At granule-scale, individual nanogranules have a strontium-rich cortex enclosing a Sr-poor aragonitic core. The four representative nanogranules shown in **b** to **e** are sized 26 to 38 nm in diameter and the widths of the Sr-enriched cortices around nanogranules are 4 to 8 nm wide, which agree well with those observed in APT. Scale bar is 200 nm.

## Supplementary Files

This is a list of supplementary files associated with this preprint. Click to download.

- [OtteretalNacreSupplementaryFinal.docx](#)
- [OtteretalNacreSupplementaryVideoCaptionFinal.docx](#)
- [OtteretalNacreSupplementaryVideoFinal.mp4](#)